





Universal nature of rapid evolution of conservative gravity and turbidity currents perturbed from their self-similar state

Santiago L. Zúñiga ^{1,2,3,*}, Jorge S. Salinas ⁴, S. Balachandar ⁴ and Mariano I. Cantero ^{1,2,3}

¹*Instituto Balseiro, Universidad Nacional de Cuyo, San Carlos de Bariloche, Argentina*

²*Centro Atómico Bariloche, Comisión Nacional de Energía Atómica, San Carlos de Bariloche, Argentina*

³*Consejo Nacional de Investigaciones Científicas y Técnicas, San Carlos de Bariloche, Argentina*

⁴*Department of Mechanical and Aerospace Engineering, University of Florida, Gainesville, Florida 32611, USA*



(Received 6 January 2022; accepted 28 March 2022; published 22 April 2022)

The results of six highly resolved direct and large eddy simulations of gravity and conservative turbidity currents are presented to illustrate the point that the rapidly varying evolution of these currents follow a universal cyclic sequence of four states. The demarcation between these four states is determined by the bulk Richardson number and the acceleration/deceleration of the flow. We describe in detail the identification process of these states, together with the associated three-dimensional structure of the current. The exact depth-averaged momentum balance is computed and used to explain the intricate details of the nonmonotonic rapid evolution of the current between the different states. Finally, the balance of turbulent kinetic energy and concentration flux are computed to explain how and why the current evolves through the cyclic sequence of states. We also explore the mechanism by which the current can exit the cyclic sequence and slowly evolve towards self-similar supercritical or subcritical states.

DOI: [10.1103/PhysRevFluids.7.043801](https://doi.org/10.1103/PhysRevFluids.7.043801)

I. INTRODUCTION

A dense underflow, below a deeper body of lighter fluid, down a sloping bottom is a configuration of considerable interest in many geophysical and engineering applications. Often the dense underflow and the lighter fluid above are the same material and the higher density is due to temperature, salinity, or suspended sediment [1,2].

The evolution of a current as it flows downstream is of fundamental importance. This evolution is controlled by four important balances [3–5]. The volume of fluid carried by the current increases due to entrainment of clear fluid at the top of the flowing current. The excess weight of the current's fluid over the surrounding is the source of streamwise momentum, which is balanced by a combination of basal drag, momentum loss by entrainment, and current acceleration. A conservative current is one where the streamwise flux of the agent responsible for the excess weight (temperature, salinity, or suspended sediment) is conserved as the current flows downstream. The fourth balance of importance is that of turbulence, which is produced, dissipated, and transported/diffused along the streamwise and bed-normal directions.

These balances have been studied using direct and large eddy simulations in the context of both the evolution of the front and the body of the current [6–15]. It is generally accepted that the head of the current is far more turbulent and considerably more erosive than the body of the current [16,17]. Even if we limit attention to the body of the current that forms behind the head, a wide variety

*santiago.zuniga@ib.edu.ar

of evolutions have been observed in simulations, laboratory experiments, and field measurements [11,18–20]. Recent simulations and experiments [5] show that, in a very long channel of constant slope, the body of a conservative current approaches a self-similar state, which is characterized by the bed slope as the only parameter. Due to the multilayer structure of the current with near-bed and interface layers [21,22], the approach to complete self-similarity is very slow and goes as x^{-1} , where x is along the flow direction. There are many situations of practical interest where the evolution of the current can be more complex [23]. For example, an oscillatory and nonmonotonic evolution of the current is observed if at the inlet of the channel the current is far from the self-similar state. The current varies rapidly during the initial adjustment immediately downstream of the inlet (rapidly varying phase), before slowly approaching the self-similar state far downstream (slowly varying phase). A similar rapidly varying phase is expected when a current is abruptly disturbed by a sudden change in the bed, such as a slope break or a localized bump, [24–26].

The demarcation between supercritical and subcritical flow is typically in terms of the local densimetric Froude number or in terms of the local Richardson number (the two are related by $Fr^2 = 1/Ri$). The supercritical and subcritical currents are defined in terms the local value of Richardson number being $Ri < 1$ and $Ri > 1$, respectively. The subcritical and supercritical nature of the current have been well characterized in their self-similar evolution. In contrast, under conditions of rapid streamwise variation, the nature of currents with local value of $Ri < 1$ and $Ri > 1$ is not well understood. The rapidly varying nonmonotonic evolution can be partitioned into four types of states: (i) accelerating current of local $Ri < 1$ (A-Super), (ii) decelerating current of $Ri < 1$ (D-Super), (iii) accelerating current of $Ri > 1$ (A-Sub), and (iv) decelerating current of $Ri > 1$ (D-Sub). As it will be shown below, the local structure of a rapidly accelerating or decelerating current of $Ri < 1$ (or $Ri > 1$) does not resemble that of self-similar supercritical (or subcritical) current. In other words, the structure of the A-Super and D-Super (or A-Sub and D-Sub) currents are distinctly different from that of self-similar supercritical (or subcritical) state that the current changes rapidly during its streamwise evolution.

The acceleration (or deceleration) status of the current is characterized by $dU/dx > 1$ ($dU/dx < 1$), where $U(x, t)$ is the span and depth-averaged streamwise velocity of the current. Since $Ri \propto U^{-2}$, a subcritical current that accelerates in a sustained manner will eventually become supercritical. That is, a current that is in A-Sub state in a sustained manner will eventually enter the A-Super state. Similarly, a supercritical current when it decelerates in a sustained manner will eventually become subcritical (i.e., a D-Super current will transition to D-Sub state). Following hydraulic literature, when the current is neither accelerating nor decelerating along the streamwise direction (i.e., $dU/dx = 0$), it will be termed *normal condition*.

The primary purpose of this work is to report our interesting observation that many (perhaps all) rapidly varying gravity currents seem to evolve in the following cyclic sequence: \dots A-Sub \rightarrow A-Super \rightarrow D-Super \rightarrow D-sub \rightarrow A-Sub $\rightarrow \dots$. The point where the current changes from the A-Super to D-Super state defines the normal supercritical (N-Super) state. Similarly the point where the current changes from the D-Sub to A-Sub state defines the normal subcritical (N-Sub) state. Though the N-Super and N-Sub states are associated with zero acceleration, they are not fixed points. They are turning points, since the balances of mass, momentum, buoyancy, and turbulence are not in perfect equilibrium. This is the reason why the current drifts between the different states.

For bed slopes $\theta > 1^\circ$, the current eventually slowly evolves to a self-similar supercritical (SS-Super) state [21]. However, depending on the status of the current at the inlet, the current will evolve through the cyclic sequence mentioned above and enter the self-similar state from the A-Super state. Similarly, for bed slopes $\theta < 1^\circ$, the current eventually slowly evolves to a self-similar subcritical (SS-Sub) state [22]. Depending on the status of the current at the inlet, the current will evolve through the cyclic sequence and enter the self-similar state from the A-Sub state. For intermediate slopes $\theta \approx 1^\circ$ the current is transcritical and the current is observed to go through the cyclic sequence several cycles without settling to a self-similar state [23].

In this work we will investigate results for several highly resolved direct and large eddy numerical simulations with up to two billion grid points. Exploring the nature of cyclic transitions between

the A-Sub, A-Super, D-Super, and D-sub states in a rapidly varying current will be the focus of this paper. We will also investigate the mechanisms of these transitions in terms of the turbulent structure of the near-bed and interface layers of the current. Our earlier efforts focused only on the structure of the supercritical and subcritical currents in the self-similar state [5,22] and on the oscillatory evolution in the transcritical state [23]. Extending these prior understandings to rapidly varying currents that are far from their self-similar state is the present focus. Of particular importance is the fact that even currents in sufficiently steep (or shallow) slopes that eventually evolve into self-similar supercritical (or subcritical) state undergo rapid oscillatory evolution when initiated or disturbed far from the self-similar state. The rapid oscillatory evolution follows a definite cyclic pattern, which will be explored here in detail.

An example of particular interest to the present work is turbidity currents where heavier sediment-laden subaqueous riverlike flows travel downstream within submarine channels. A turbidity current is heavier than the surrounding body of water due to the suspended sediment. Often the suspended sediment is noncohesive and small enough so that its settling velocity can be ignored. In the absence of deposition or erosion of sediments at the bottom of the current, the turbidity current behaves essentially as a *conservative gravity current*.

The rest of the paper is organized as follows. In Sec. II we present the simulation details and the numerical model. In Sec. III we precisely define the four different rapidly varying states. The three-dimensional structure of the current at each state is shown and analyzed in Sec. IV. We compute the depth-averaged momentum, turbulent kinetic energy, and concentration balances in Secs. V and VI. While the previous sections used the results of two simulations as primary examples of illustration, in Sec. VII we consider four other cases of rapidly varying currents to demonstrate the universal nature of the cyclic evolution between the four states. Finally, in Sec. VIII we discuss in detail the consequences of cyclic evolution between the four different states in terms of turbulence and concentration flux partitioning between the near-bed and interface layers.

II. SIMULATION DETAILS AND CASES STUDIED

In the following, we report on six direct and large eddy simulations of gravity currents flowing down a sloping bed of inclinations between $\theta = 0.29^\circ$ and 2.9° . The density variation is assumed to be sufficiently small that the use of the Boussinesq approximation is valid. With this assumption, the governing equations are

$$\frac{\partial \mathbf{u}}{\partial t} + \mathbf{u} \cdot \nabla \mathbf{u} = -\nabla p + \frac{1}{\text{Re}_{\text{in}}} \nabla^2 \mathbf{u} + \text{Ri}_{\text{in}} c \mathbf{e}_g, \quad (1)$$

$$\nabla \cdot \mathbf{u} = 0, \quad (2)$$

$$\frac{\partial c}{\partial t} + \mathbf{u} \cdot \nabla c = \frac{1}{\text{Re}_{\text{in}} \text{Sc}} \nabla^2 c, \quad (3)$$

where $\mathbf{e}_g = (\sin \theta, 0, -\cos \theta)$, with θ being the bed slope. The equations are nondimensionalized with the inlet half-height H as the length scale, average concentration of the agent responsible for the excess buoyancy at the inlet plane $c_v = 1/2H \int_0^{2H} \tilde{c} dz$ as the concentration scale, and inlet average velocity $U_{\text{in}} = 1/2H \int_0^{2H} \tilde{u} dz$ as the velocity scale. With these scales, the dimensionless parameters are the inlet Reynolds number $\text{Re}_{\text{in}} = U_{\text{in}} 2H / \nu$, Schmidt number $\text{Sc} = \nu / \kappa$, where ν is the fluid kinematic viscosity and κ is the concentration diffusivity, and inlet Richardson number $\text{Ri}_{\text{in}} = R g c_v 2H / U_{\text{in}}^2$. Here, g is the acceleration due to gravity and $R = \rho_s / \rho_f - 1$, where ρ_s and ρ_f are the densities of the agent of excess buoyancy being transported and the fluid, respectively. For all the cases studied in the present work, $\text{Re}_{\text{in}} = 5650$ and $\text{Sc} = 1$.

Cases 1 and 3 through 6 have a constant bed slope θ , while case 2 presents a slope-break at $x = 231$ where θ changes. The intent of the slope break is to induce a rapid transition between a self-similar subcritical state (SS-Sub) to a supercritical state (SS-Super) and observe the transition

TABLE I. Details of cases studied in this work. Case name, slope angle, inlet Richardson number, domain size, number of spectral elements, and number of GLL point per element. For all cases, $Re_{in} = 5650$ at the inlet. Directions x , y , and z correspond to streamwise, spanwise, and wall-normal directions, respectively.

Case	θ	Ri_{in}	$L_x \times L_y \times L_z$	$N_{e,x} \times N_{e,y} \times N_{e,z}$	N_p
Case 1	0.72°	0.66	$301 \times 8\pi/3 \times 20$	$336 \times 16 \times 44$	8^3-16^3
Case 2	0.29° in $x \in [0, 231)$ 2.9° in $x \in [231, 580]$	1.62	$580 \times 8\pi/3 \times (12-30)$	$612 \times 16 \times 40$	8^3-16^3
Case 3	0.29°	0.33	$904 \times 8\pi/3 \times 20$	$504 \times 8 \times 30$	8^3
Case 4	0.29°	1.28	$904 \times 8\pi/3 \times 20$	$504 \times 8 \times 30$	8^3
Case 5	0.29°	2.83	$904 \times 8\pi/3 \times 20$	$504 \times 8 \times 30$	8^3
Case 6	2.9°	1.42	$904 \times 8\pi/3 \times 20$	$504 \times 8 \times 30$	8^3

between the two. Cases 1 and 2 are high resolution DNS simulations, whereas cases 3 through 6 are LES simulations with a dynamic Smagorinsky model implementation [27,28]. For the DNS simulations, the grid resolution in wall units is up to $\Delta x^+ \simeq 5$, $\Delta y^+ \simeq 3$, and $\Delta z_{wall}^+ \simeq 0.3$ for the streamwise, spanwise, and wall-normal directions, respectively. For LES cases, $\Delta x^+ \simeq 20$, $\Delta y^+ \simeq 12$, and $\Delta z_{wall}^+ \simeq 0.7$. At the inlet plane, for $z \leq 2$, all simulations use synthetic turbulence generation based on the synthetic eddy method [29,30]. The velocity data for the inlet plane is based on a turbulent channel flow with $Re = 5650$ [31] and constant concentration $c(0, y, z \leq 2) = 1$. For $z > 2$, the inlet velocities are set equal to zero. At the top boundary condition, far from the top edge of the current, the computational domain is open and allows for ambient fluid to enter the domain to compensate for clear water entrainment in the current. The outlet boundary consists of a stabilized open boundary condition [32], allowing for the current to exit the domain. Statistics were taken for at least 200 nondimensional time units after reaching statistical equilibrium, which corresponds to approximately 10^5 time steps. (See Table I.)

III. FOUR DIFFERENT RAPIDLY VARYING STATES

We start with a precise characterization of the four different rapidly varying states of the current. We will use the simulation results of case 1 and case 2 for this purpose. Local Richardson number is defined as

$$Ri(x) = \frac{1}{Fr(x)^2} = \frac{h_u^2 Ri_{in} \int_0^\infty \bar{c} dz}{\left(\int_0^\infty \bar{u} dz\right)^2}, \quad (4)$$

where h_u is the upper edge of the current defined by the location where streamwise velocity is nearly zero ($\bar{u} = 2 \times 10^{-2}$, $\sim 0.1\%$ of the velocity maximum). In all the cases considered, the flow is homogeneous along the spanwise direction and statistically stationary and as a result the ensemble average is approximated by an average over spanwise direction and time and denoted by an overbar. With the above definition, the Richardson number is a function of the streamwise direction x . Figure 1 shows a plot of Ri versus x for all cases considered. We also define the gradient Richardson number as the ratio between the stabilizing effect of stratification and the destabilizing effect of shear,

$$Ri_g(x) = -Ri_{in} \frac{\partial \bar{c} / \partial z}{(\partial \bar{u} / \partial z)^2}, \quad (5)$$

where the numerator is the nondimensional Brunt-Väisälä frequency $N^2 = -Ri_{in} \partial \bar{c} / \partial z$. Also plotted in Fig. 1 is the local minimum gradient Richardson number Ri_g within the interface defined as $Ri_{g,min}(x) = Ri_g(x, z)|_{\min}$ for $z > z_{um}$, where $z_{um}(x)$ is the vertical location of span and time averaged streamwise velocity peak, for each streamwise location x . Thus, at each streamwise location, the

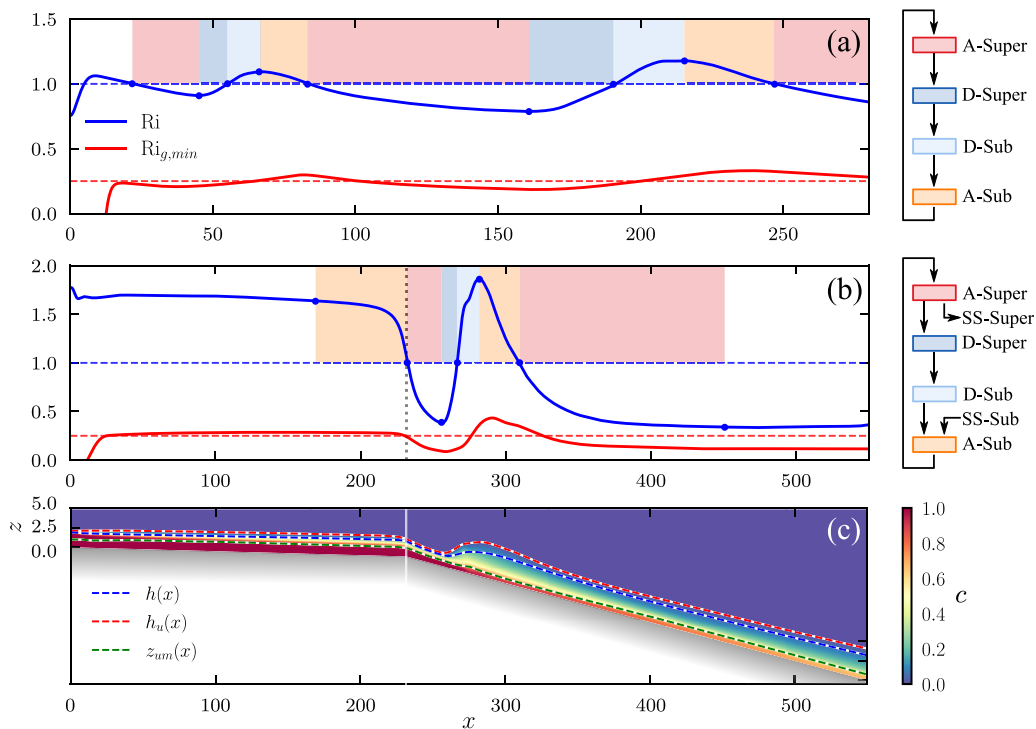


FIG. 1. (a), (b) bulk Richardson number Ri and the local minimum value of the gradient Richardson number Ri_g within the interface layer for (a) case 1 and (b) case 2. Colors denote the non-normal regime at each streamwise location. (c) Spanwise and time averaged concentration field for case 2. Also shown are current thickness $h(x)$, upper edge of the current defined by the location of zero streamwise velocity $h_u(x)$, and the location of the streamwise velocity maximum $z_{um}(x)$. Wall normal axis is stretched for better visualization.

minimum value of the gradient Richardson number is chosen within the upper interface layer. In the plots of Richardson number, we identify the following four states of current evolution: *A-Super*: regions where $Ri < 1$ and $d Ri/dx < 0$ (shaded red); *D-Super*: regions where $Ri < 1$ and $d Ri/dx > 0$ (blue); *D-Sub*: regions where $Ri > 1$ and $d Ri/dx > 0$ (light blue); *A-Sub*: regions where $Ri > 1$ and $d Ri/dx < 0$ (orange). Furthermore, we observe the occurrence of the sequence \dots A-Sub \rightarrow A-Super \rightarrow D-Super \rightarrow D-sub \rightarrow A-Sub $\rightarrow \dots$ as a natural consequence of the periodic evolution of the Richardson number.

Although the two cases shown in the figure are qualitatively similar, the quantitative evolution of Ri is different both in the amplitude and in the wavelength of variation. In case 1 [Fig. 1(a)], the Richardson number of the transcritical current remains close to unity and thus the amplitude of cyclic variation is not large. On the other hand, in case 2 [Fig. 1(b)], as the slope changes, the self-similar Richardson number corresponding to these slopes changes from about 1.7 to 0.35, and this change occurs following the cyclic sequence. Furthermore, in case 2, after one and a half cycles the current enters a slow approach towards SS-Super state, whereas in case 1 the current continues to cyclically vary till the end of the computational domain.

A few other features can be readily identified as well. First and foremost, the extent of deceleration is typically much shorter than the extent of acceleration. As will be seen in the three-dimensional structure of the current, the deceleration phase is associated with an internal hydraulic jump and an increase in the height of the current with vigorous generation of turbulent structures within the current. Therefore, the streamwise extent of deceleration is typically limited, especially when compared to the much gentler evolution of the current during the acceleration phase.

The difference can also be understood in terms of streamwise pressure gradient. Deceleration is associated with positive streamwise pressure gradient and the rapid change of the current is in response to this adverse pressure gradient. In comparison, acceleration is associated with favorable streamwise pressure gradient and the flow evolves smoothly.

Also plotted in the figure is the local minimum value of gradient Richardson number Ri_g within the interface layer as a function of x , whose behavior is similar to the bulk Richardson number in that it oscillates around the critical number $Ri_g = 0.25$ [33]. Streamwise locations where $Ri_g > 0.25$ imply that the entire interface layer is stabilized by stable stratification, whereas regions where $Ri_g < 0.25$ correspond to locations where some portion of the interface layer supports shear instability. Although $Ri_g = 0.25$ is the traditionally accepted critical value [33], we caution the reader that $Ri_g = 0.25$ does not demarcate stable and unstable regimes. We observe that, in the currents to be discussed in this work, $Ri_g = 0.25$ seems to be reasonably accurate in separating stable and unstable behavior of the interface layer, although the precise critical value sometimes seems to deviate. Furthermore, it must be stressed that a local value of $Ri > 1$ does not indicate $Ri_g > 0.25$ and stability of the upper interface layer. While this relation may be appropriate in the self-similar state, it does not apply when the flow is rapidly evolving. We observe a phase lag between Ri_g and Ri , which is related to the lag between dissipation and production of turbulent kinetic energy. That is, the interface turbulence takes a while to dissipate after Ri_g increases above 0.25.

Figure 1(c) shows a spanwise and time averaged concentration field for case 2 and the downstream evolution of the current thickness defined as [34]

$$h(x) = \frac{\left(\int_0^\infty \bar{u} dz\right)^2}{\int_0^\infty \bar{u}^2 dz}. \quad (6)$$

Also shown are the upper edge of the current $h_u(x)$ and the location of the streamwise velocity maximum z_{um} . Here we observe that, immediately after the slope change, the current thickness slightly diminishes accompanied by downstream acceleration, followed by an internal hydraulic jump with a sudden increase in the current height and strong deceleration. Over the entire streamwise length, the height of the current $h(x)$ is a little lower than the current edge $h_u(x)$, defined by the point of zero streamwise velocity. Also, the location of velocity maximum $z_{um}(x)$ is much closer to the bed compared to the current height.

The streamwise evolution of the velocity and concentration profiles for cases 1 and 2 are presented in Fig. 2. Also marked in the figure as a blue dashed line is the location of velocity maximum that separates the lower near-bed layer from the interface layer above [21,22]. In case 1, a small oscillatory adjustment of the current along the streamwise direction is observed. The cumulative effect of the changes from $x = 20$ to 260 is quite significant for both the velocity and concentration profiles. Case 2 shows the transition from a subcritical to a supercritical current, where the velocity and concentration profiles at $x = 200$ and 500 match the corresponding experimental velocity and concentration profiles measured in the subcritical and supercritical self-similar-like regimes, respectively [12,19,35–37]. The oscillatory evolution of the current that was clear in the Ri plots is not entirely evident in these profiles. We do observe some influence of the cyclic evolution in the profiles, for example, around $x = 275$ in case 2.

IV. THREE-DIMENSIONAL STRUCTURE

Figures 3 and 4 show composite plots for cases 1 and 2, respectively, where the turbulent structures captured by isosurfaces of swirling strength ($\lambda_{ci} = 4$ above and $\lambda_{ci} = 10$ below z_{um}) [38,39] are colored by bed-normal location z , together with bottom and top isosurfaces where turbulent kinetic energy (TKE) production is zero (light blue and pink surfaces). Moreover, the interface between the current and the ambient is shown by an isosurface of concentration $c = 0.01$ (light brown). Note that, for case 1 (Fig. 3), regions above and below z_{um} are separately presented with different color scales for better visualization. Also in this plot we present contours of spanwise

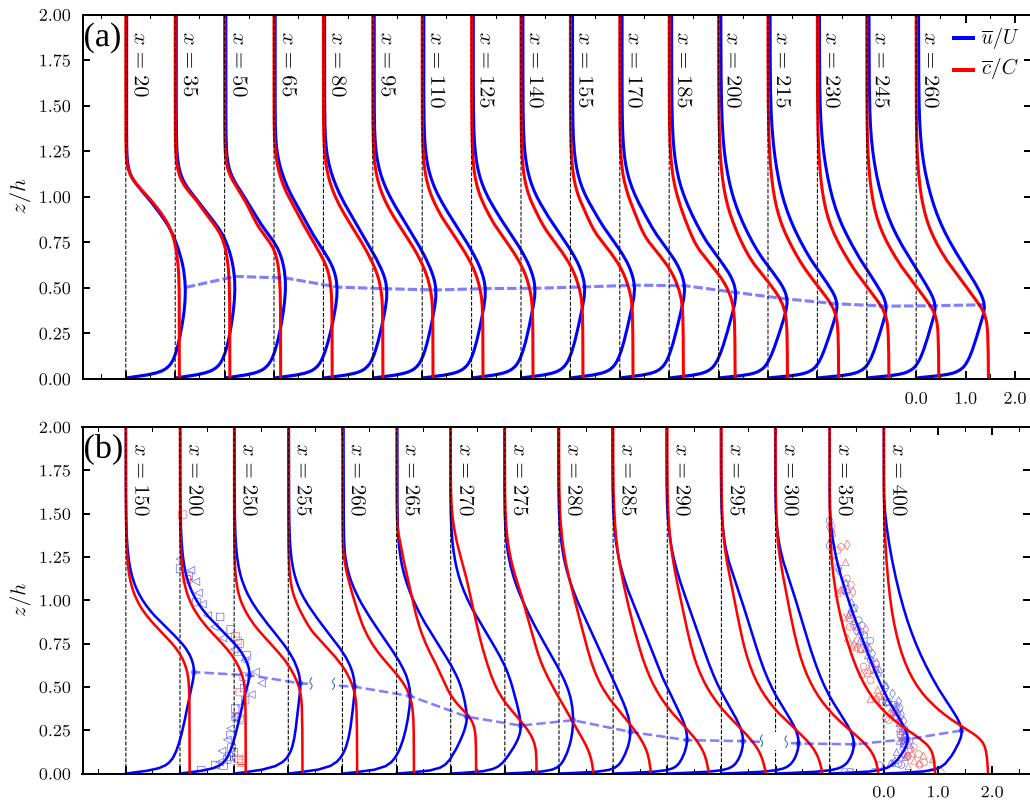


FIG. 2. Scaled velocity and concentration profiles at different downstream locations for (a) case 1 and (b) case 2. Experimental and field data points from \square [19], \triangleleft [35], \circ [36], \triangle [37], and \diamond [12]. Blue and red symbols correspond to velocity and concentration profiles, respectively. The dashed blue line corresponds to $z_{um}(x)$.

vorticity Ω_y in the plane $y = 1.95$ (red-blue color scale), shown only in the region ($c \leq 0.01$) and stretched in the bed-normal direction for better visualization. Also shown are contours of zero TKE production (light yellow) to illustrate the two/three layer structure of the current. We will focus on the region $120 < x < 280$ for case 1 [see Fig. 1(a)] and $200 < x < 440$ for case 2 [see Figs. 1(b) and 1(c)], where we can analyze a complete cycle through all the states.

We will use case 1 to first describe the structural evolution of the current through the sequence of states (see Fig. 3). At $x = 120$ the current is in A-Super state; the interface between the ambient and the current is mainly flat, with an absence of turbulent structures in the interface layer. The contours of spanwise vorticity resemble those seen in a self-similar subcritical gravity current [5,22]. Thus it must be noted that, although the current is closer to a self-similar subcritical current in terms of its turbulent structure, its momentum and buoyancy correspond to those of a supercritical current. This inconsistency arises because immediately upstream the current was in A-Sub state, and it rapidly accelerated to become A-Super. While the rapid evolution of the current was sufficient to change the local Richardson number to be below 1, the turbulent structures still remain the same as those of a subcritical current. This imbalance is important, since it forces the current to evolve to the next stage. As a result, in the A-Super state, we observe a three layer structure similar to a self-similar subcritical current (see frame D of the schematic shown in Fig. 7), where the intermediate layer results from the counter-rotating vortices (CV) above the heads of near-bed hairpin vortices that point downstream and up (HP_b). This intermediate layer exists between the near-bed and interface

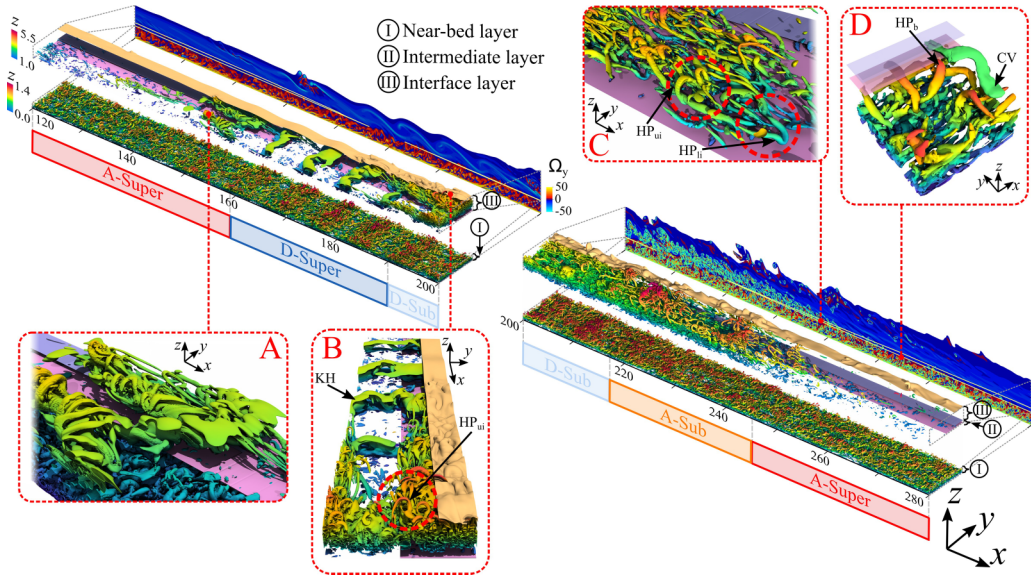


FIG. 3. Three-dimensional structure of case 1. Turbulent structures in the density current are captured by an isosurface of swirling strength ($\lambda_{ci} = 4$ at interface and $\lambda_{ci} = 10$ at near-bed layer) and colored by wall normal location z , together with bottom and top isosurfaces where TKE production is zero (light blue and pink surfaces). Also shown are contours of spanwise vorticity Ω_y at $y = 1.95$ (red-blue color scale). Moreover, contours of zero TKE production at $y = 1.95$ are shown in light yellow. Colors of bottom labels denote the rapidly varying state at each streamwise location.

layers, presenting negative TKE production which acts as a barrier for momentum and turbulence transfer between layers.

Towards the end of the A-Super state, as a result of the cumulative acceleration of the current, the stabilizing effect of stratification has significantly decreased and packets of hairpin vortices start forming at the top of the interface layer ($150 \lesssim x \lesssim 160$; see inset A in Fig. 3). However, the

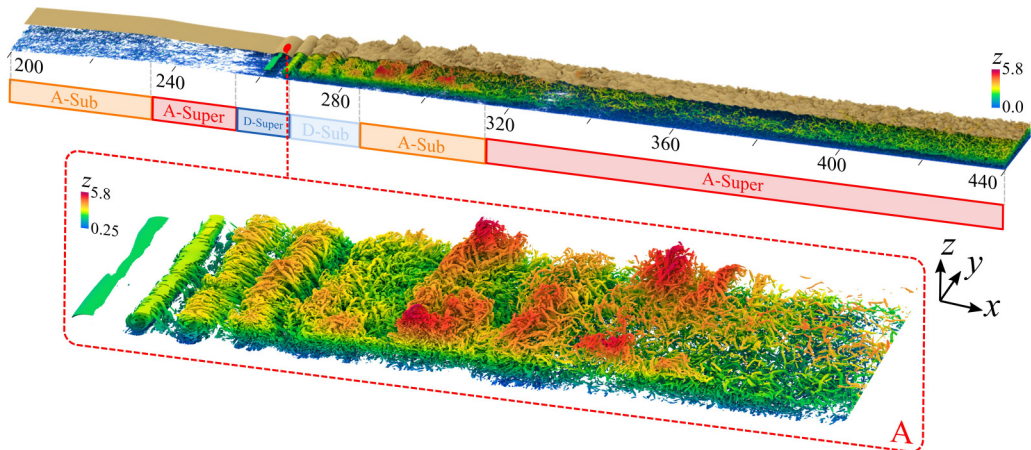


FIG. 4. Three-dimensional structure of case 2. Turbulent structures in the density current are captured by an isosurface of swirling strength $\lambda_{ci} = 4$ and colored by wall normal location z . Colors denote the rapidly varying state at each streamwise location.

intermediate layer with negative TKE production is still present and there is no interaction between structures in the near-bed and interface layers. Furthermore, spanwise vorticity is mostly negative (counterclockwise rotation) in the intermediate and interface layers, while the near-bed layer is populated by hairpin vortices.

Further downstream, at $x \approx 170$, the current starts to decelerate and enter the D-Super regime. As a result of weakened stratification effect, shear-induced, spanwise coherent structures start forming, which subsequently give a wavy structure to the interface (KH on inset B). The intermediate layer with negative TKE production disappears. This can be seen by the end of the light blue plane indicating that $\bar{P} \geq 0$ in the entire current. Furthermore, the thinning and subsequent absence of the intermediate layer is accompanied by interaction between the near-bed (HP_b) and interface structures, where hairpin vortices that populate the near-bed layer tilt their head down, right below the spanwise coherent interfacial vortices (KH), and up in the regions between these.

With enhanced entrainment, a larger fraction of the driving potential energy is lost to interfacial drag. Therefore, the current slows down and enters D-Sub state. Around $x \approx 190$ spanwise coherent vortices start breaking down into smaller structures which give the tonguelike structure of the interface (HP_{ui} on inset B). The current acquires a two layer structure (near-bed and interface layers) where three families of hairpin vortices are found: (i) near-bed hairpin vortices HP_b below z_{um} ; (ii) lower-interface hairpin vortices HP_{li} right above z_{um} ; (iii) upper-interface hairpin vortices HP_{ui} near the current-ambient interface [21]. A schematic representation of this transition can be seen in inset C.

Again, we observe that, in the D-Sub state, although the current is closer to a self-similar supercritical current in terms of its turbulent structure (three families of hairpin vortices populate the current), its momentum and buoyancy are corresponding to those of a subcritical current. This is because, while the current has rapidly decelerated to a local Richardson number higher than 1, turbulent structures still remain the same as those of a supercritical current. This imbalance forces the current to evolve to the next stage. As the current travels downstream and stratification increases, fewer structures are seen in the interface layer. An interesting separation of the upper interface structures can be seen by analyzing the contours of $\lambda_{ci} = 4$ (in green) presented together with spanwise vorticity contours. As stratification increases, the upper interface structures decrease in height, up until a point where the upper HP_{ui} and lower HP_{li} interface structures are close to each other at $x \approx 250$ (A-Sub state; see inset C). At the same time, some weaker structures are remnant near the current-ambient interface, which widen their interlib angle as they travel downstream until they dissipate. After these isolated vortices HP_{ui} dissipate, hairpin vortices populate the current only in the near-bed layer (HP_b on inset D). This transition from turbulent to nonturbulent interface layer happens together with the formation of the intermediate layer of negative TKE production. Moreover, after the interface becomes nonturbulent ($x \gtrsim 250$), spanwise vorticity becomes mainly negative.

The evolution of turbulent structures in case 2 (see Fig. 4) is quite similar to that seen in case 1. However, case 2 is useful to reinforce the point that the specific interface characteristics are strongly influenced by the upstream state. For example, the A-Super state at $x \approx 240$ in case 2 is similar to the A-Super state in case 1 at $x \approx 140$. The subsequent evolution of vortical structures in both cases is similar as well. However, the A-Super state in case 2 at $320 < x < 450$ does not show a flat interface since, unlike in case 1, turbulence does not decay away in the interface layer. Instead of being in a supercritical state without interfacial turbulence, the current transitions to a slow acceleration and evolves to a self-similar supercritical state with the appropriate amount of turbulence in the interface layer for a supercritical state. Also of interest is how the interface turbulence develops as shown in inset A. We see the classic formation of initial two-dimensional Kelvin-Helmholtz rollers that undergo three-dimensional instability with the formation of streamwise ribs that reside in the braid region between the Kelvin-Helmholtz rollers [40,41], which quickly break down into interface turbulence. The high resolution of the DNS is essential in resolving the resulting complex vertical structure.

V. MOMENTUM AND TKE BALANCES

Following [3,42,43] we first investigate the dimensionless span and depth-averaged mean streamwise momentum equation. In the present case of steady flow regime, the mean streamwise momentum balance can be rigorously expressed in the following form without any approximation [5]:

$$\text{Ri}_{\text{in}} \sin \theta \int_0^\infty \bar{c} dz - \frac{1}{\text{Re}_{\text{in}}} \left(\frac{\partial \bar{u}}{\partial z} \Big|_{z=0} + \frac{d^2 Q}{dx^2} \right) - \frac{\partial}{\partial x} \int_0^\infty \bar{p} dz - \frac{\partial}{\partial x} \int_0^\infty \overline{u'u'} dz - \frac{\partial}{\partial x} \int_0^\infty \bar{u}^2 dz = 0, \quad (7)$$

where the streamwise fluxes of mass, momentum, and buoyancy are defined as

$$Q(x) = \int_0^\infty \bar{u} dz, \quad M(x) = \int_0^\infty \bar{u}^2 dz, \quad F(x) = \int_0^\infty R\bar{c}\bar{u}g \sin \theta dz. \quad (8)$$

In the simulations, the upper limit is replaced with a large value of z that extends far upwards into the ambient, where the current velocity and buoyancy vanish. The fluxes are used to define current height $h(x) = Q^2/M$ and mean velocity $U(x) = M/Q$. Following the steps presented in [5] the momentum balance can be rewritten as

$$\frac{FQ}{\theta_m M} - C_D \frac{M^2}{Q^2} - \frac{d(\beta_p M)}{dx} - \frac{d(\beta_f M)}{dx} - e_w \frac{M^2}{Q^2} - Q \frac{dU}{dx} = 0, \quad (9)$$

where the first four terms correspond to the first four terms of (7) and the last two terms correspond to the last term of (7). In the above momentum balance, $C_D(x)$ is the basal drag coefficient, $e_w(x)$ is the entrainment coefficient, and $\theta_m(x)$, $\beta_p(x)$, and $\beta_f(x)$ are $O(1)$ shape factors, whose definitions and values in the self-similar regime are given in [5].

The first term in (9) accounts for the excess weight due to concentration and is the source of streamwise momentum. It is balanced by the other five terms, which in order represent the net viscous drag force on the current, streamwise pressure gradient force, streamwise Reynolds stress effect, the cost of raising the streamwise velocity of the entrained fluid from zero to U , and the acceleration of the current. Note that $C_D M^2/Q^2$ and $e_w M^2/Q^2$ are guaranteed to be positive and therefore viscous drag and entrainment effects are dissipative. In contrast, the other three terms can be a moment sink or source. In particular, when $QdU/dx > 0$, it absorbs momentum while accelerating (acts as a sink) and releases momentum while decelerating (acts as a source).

Figures 5(a) and 5(b) show the depth-averaged momentum balance, Eq. (9), as a function of streamwise location x for case 1 and case 2, divided by M^2/Q^2 for nondimensionalization. Let us first focus on the downstream section when the current is in the A-Super and D-Super states [red and dark blue shaded regions in Fig. 5(a)]. As the current travels downstream, as indicated by the sign of $-(Q^3/M^2)du/dx$, the acceleration of the current decreases and begins to decelerate rapidly, reaching the maximum deceleration at the end of D-Sup. During this period, stratification decreases and the interface layer is increasingly turbulent. With this, ambient fluid entrainment increases as indicated by the negative peak of $-e_w$ (purple line) as a result of enhanced interfacial mixing. However, basal shear stress (green line) remains nearly unchanged indicating that the rapid evolution is mainly limited to the turbulent nature of the upper interface layer. As can be expected, streamwise pressure gradient $[(Q^2/M^2)d(\beta_p M)/dx]$ becomes negative during periods of acceleration, and becomes positive during periods of deceleration. The periods of positive streamwise pressure gradient also coincide with the appearance of spanwise coherent interfacial vortices. This corresponds to internal hydraulic jumps [44], where potential energy increases due to the increase in the current's height at the expense of kinetic energy. The Reynolds stress contribution $[(Q^3/M^2)d(\beta_f M)/dx]$, although small, behaves similar to the streamwise pressure gradient.

Focusing on streamwise sections when the current is in the D-Sub and A-Sub states [light blue and orange shaded regions in Fig. 5(a)], as the current travels downstream, momentum is lost/gained to accelerate/decelerate the flow and stratification increases resulting in a decrease in ambient fluid entrainment. Only a slight increase in bed shear stress can be observed. With the

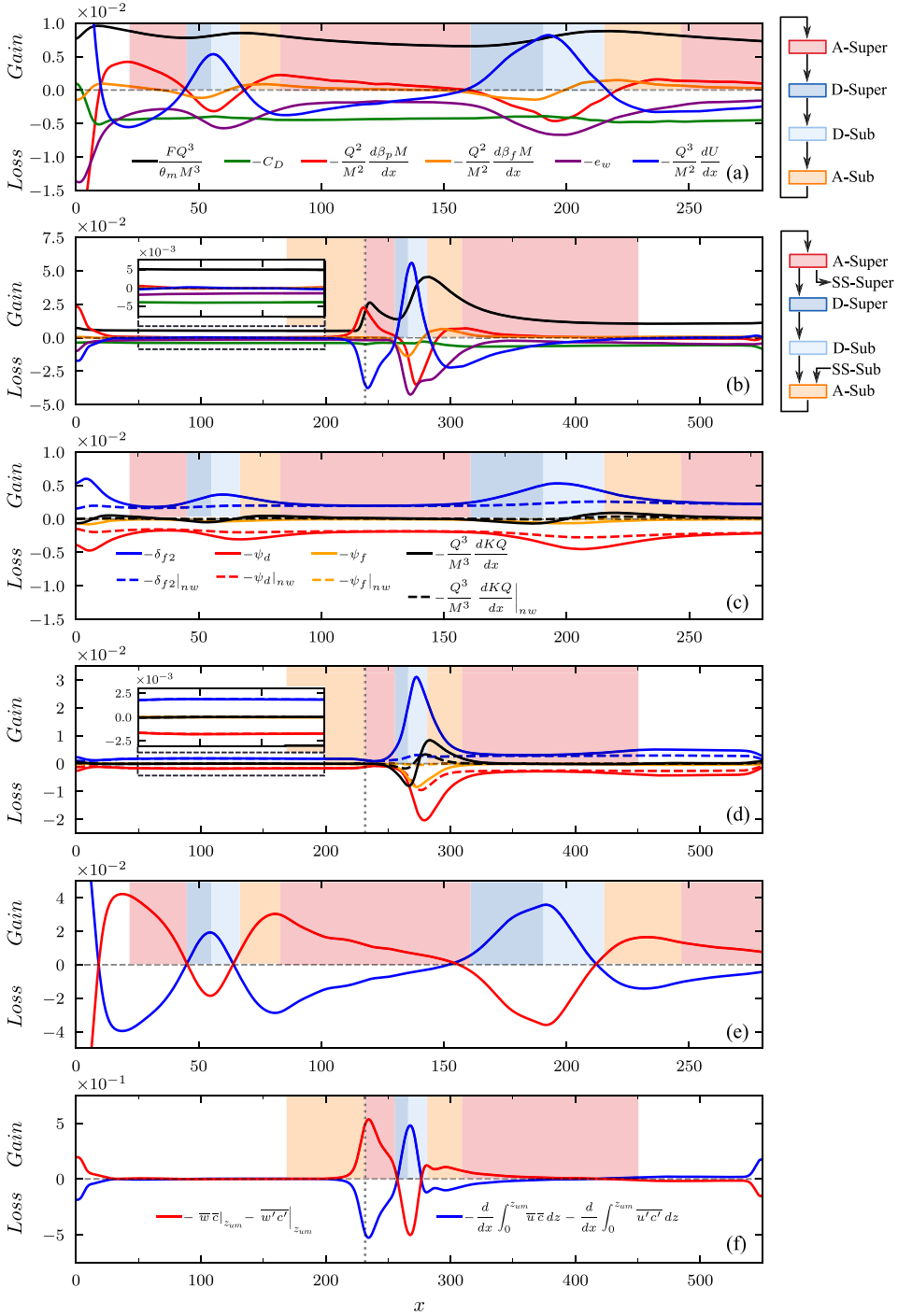


FIG. 5. Scaled depth-averaged momentum balance as a function of downstream location x for (a) case 1 and (b) case 2. Scaled depth-average TKE balance as a function of downstream location x , for (c) case 1 and (d) case 2. Dashed lines show the depth-average terms integrated up until the velocity maximum (near-bed balance). Balance of scaled concentration flux as a function of downstream location. (e) Near-bed balance for case 1. (f) Near-bed balance for case 2.

enhanced stratification, the interface is stable again, and the streamwise pressure gradient changes from positive to negative. Finally, in this transition from turbulent to nonturbulent interface layer, momentum is gained through the Reynolds stress term as well.

It is striking to observe that, at the normal points of zero acceleration, where the current changes from acceleration to deceleration or deceleration to acceleration, the other streamwise variation terms are zero as well [i.e., $(Q^3/M^2)d(\beta_p M)/dx \approx 0$ and $(Q^3/M^2)d(\beta_f M)/dx \approx 0$ as well]. In other words, the normal points are also fixed points of the current evolution, where the momentum source is nearly balanced by viscous drag at the bottom and entrainment drag at the interface with the ambient fluid. However, these fixed points are unstable and the current quickly transitions from A-Super to D-Super state and from D-Sub to A-Sub state, without remaining at the normal condition, i.e., the condition where the current does not accelerate or decelerate downstream. It should be noted that the points of zero streamwise acceleration (i.e., at $x = 44, 68, 158,$ and 216 when $dU/dx = 0$) are associated with nonzero d^2U/dx^2 and thus the current continues to exhibit cyclic evolution.

In contrast, in case 2, the current evolves from near subcritical self-similar state to self-similar supercritical state and thus perfect equilibrium of the momentum balance can be seen for $100 < x < 200$ and $450 < x < 500$ in Fig. 5(b). As expected, streamwise acceleration is negligible at both terminal states. Also, the streamwise changes in pressure and Reynolds stress contributions are negligible. As a result, the streamwise momentum source is balanced by losses due to shear stress at the bed and ambient fluid entrainment. During the rapid evolution, the current attains normal condition (i.e., $dU/dx = 0$) at $x = 255, 285,$ and 450 . While the former two are unstable and associated with $d^2U/dx^2 \neq 0$, the approach to the final normal condition is a slowly varying self-similar state. In the supercritical self-similar state $C_D \approx e_w$, while in the rapidly evolving states one or the other has a dominant contribution.

We now explore the cyclic variation in interfacial turbulence by investigating the turbulent kinetic energy (TKE) balance. The dimensionless mean TKE balance in the statistically stationary state can be expressed as

$$\int_0^\infty \bar{P} dz - \int_0^\infty \bar{\varepsilon} dz - \text{Ri}_{\text{in}} \cos \theta \int_0^\infty \overline{w'c'} dz - \frac{\partial}{\partial x} \int_0^\infty \bar{u}k dz \approx 0. \quad (10)$$

The first two terms are the TKE production and dissipation, where $\bar{P} = -\overline{u'_i u'_j} \frac{\partial \bar{u}_i}{\partial x_j}$ and $\bar{\varepsilon} = \frac{1}{\text{Re}_{\text{in}}} \overline{\frac{\partial u'_i}{\partial x_j} \frac{\partial u'_i}{\partial x_j}}$, where the overbar indicates span and time average and the prime indicates fluctuation about this mean. The other two terms are the wall-normal Reynolds flux and streamwise convection of TKE. Introducing shape factors as in the momentum equation, the above TKE balance can be rewritten as (see [5])

$$\delta_{f2} \frac{M^3}{Q^3} - \psi_d \frac{M^3}{Q^3} - \psi_f \frac{M^3}{Q^3} - \frac{dKQ}{dx} \approx 0, \quad (11)$$

where δ_{f2} , ψ_d , and ψ_f are shape factors.

Unlike the streamwise momentum equation (9), which was exact, the above TKE equation is approximate since it ignores viscous diffusion and transport terms. As we will see below, the contributions of these additional terms that are neglected in the above balance are in general quite small. The above integrals are over the entire layer and thus the production, dissipation, and the other terms account for turbulence balance within both the near-bed layer and in the interface layer. In order to investigate the TKE balance within each of these two layers separately, we will recompute the above four terms by replacing the integrals to cover only the near-bed layer. For example, the near-bed production will be calculated as $\delta_{f2}|_{nw}(M^3/Q^3) = \int_0^{z_{um}} \bar{P} dz$. The difference $\delta_{f2}| - \delta_{f2}|_{nw}$ thus represents turbulence production in the interface layer. The vertical position of the maximum streamwise velocity, z_{um} , nearly coincides with the location of the intermediate layer, defined as the region with zero or negative turbulent production [22], and demarcates the boundary between near-bed and interface layers. The height of the intermediate layer is small compared to the total current height and its contribution to the integrals defined above is negligible.

Figures 5(c) and 5(d) show the different terms of the TKE balance as a function of streamwise location x , for cases 1 and 2. Focusing on case 1 at $x = 120$ (A-Super state), the only non-negligible contributions to the TKE budget are the near-bed production and dissipation. As stratification within the interface layer decreases, TKE production increases and this increase is primarily in the interfacial layer. Note that the TKE production term appears in the mean flow kinetic energy equation as a sink. This means that, as the flow decelerates in the D-Super state, energy is taken from the mean flow and spent in generating interfacial turbulence. There is a streamwise lag between turbulence production and dissipation, with the peak dissipation in the interface layer occurring at $x \approx 210$ downstream of peak production at $x \approx 190$. Thus, downstream of where the interface is vigorously turbulent, the smaller scales of turbulence start to dissipate rapidly. Moreover, this imbalance between production and dissipation results in streamwise advection of TKE (black line) and expenditure of TKE in interface Reynolds flux (orange line). Now focusing on the extinction of interface turbulence we see that after $x \approx 220$ (A-Sub state), as the flow starts accelerating, kinetic energy of the mean flow increases. TKE dissipation is high and is not balanced by the decreasing TKE production. As a result, streamwise advection of TKE becomes positive to balance the excess dissipation. Finally, as the interface turbulence is again suppressed by stratification, Reynolds flux becomes negligible and the TKE balance becomes mainly between near-bed TKE production and dissipation.

VI. PARTITIONING OF CONCENTRATION FLUX

Figures 5(e) and 5(f) present the depth-averaged balance given by the two terms

$$\frac{d}{dx} \int_0^{z_{um}} (\overline{uc} + \overline{u'c'}) dz + (\overline{wc}|_{z_{um}} + \overline{w'c'}|_{z_{um}}) \approx 0 \quad (12)$$

as a function of downstream location x for cases 1 and 2. These two terms represent the streamwise variation in total concentration flux of the agent responsible for excess weight (mean plus Reynolds) within the near-bed layer and the vertical transport from the near bed to the interface layer. As can be seen in Figs. 5(e) and 5(f), these two terms nearly balance, indicating that any increase (or reduction) in streamwise concentration flux in the near-bed layer is due to concentration entering (or leaving) the near-bed layer from above—note that there is zero concentration transport across the bottom boundary.

The above equation describes the balance of concentration flux in the near-bed layer and a similar equation can be written for balance of concentration flux in the interface layer. The second term of (12) appears in the balance of the interface layer with an opposite sign. In other words, concentration that enters (or leaves) the near-bed layer must come from (enter into) the upper interface layer, which in turn will affect the streamwise flux of concentration in the interface layer. Thus Figs 5(e) and 5(f) are appropriate for both the near-bed and interface layers. From the figure, it is clear that during flow acceleration, especially during peak acceleration when the current transitions from A-Sub to A-super state, concentration is leaving the interface layer. On the other hand, during peak deceleration when the current transitions from D-Super to D-sub state, concentration is up-welled into the interface layer from the near-bed layer due to large-scale interfacial instabilities.

The exchange of concentration between the two layers follows the same pattern in case 2 as well. However, in this case, the flow starts in the self-similar subcritical state with perfect balance between the carrying capacities of the two layers. With the change of slope, however, this equilibrium is disrupted. The current goes through the cyclic evolution of the four different states while exchanging concentration between the interface and the near-bed layers. The net effect of these back and forth exchanges is that the near-bed layer loses concentration to the interface layer, which becomes turbulent in its approach to the self-similar supercritical state. Therefore, the interface layer is able to carry a larger amount of concentration.

In the self-similar state there is little exchange of concentration between the two layers, as indicated in Fig. 5(f) well before and after the slope change. In fact, in the self-similar subcritical

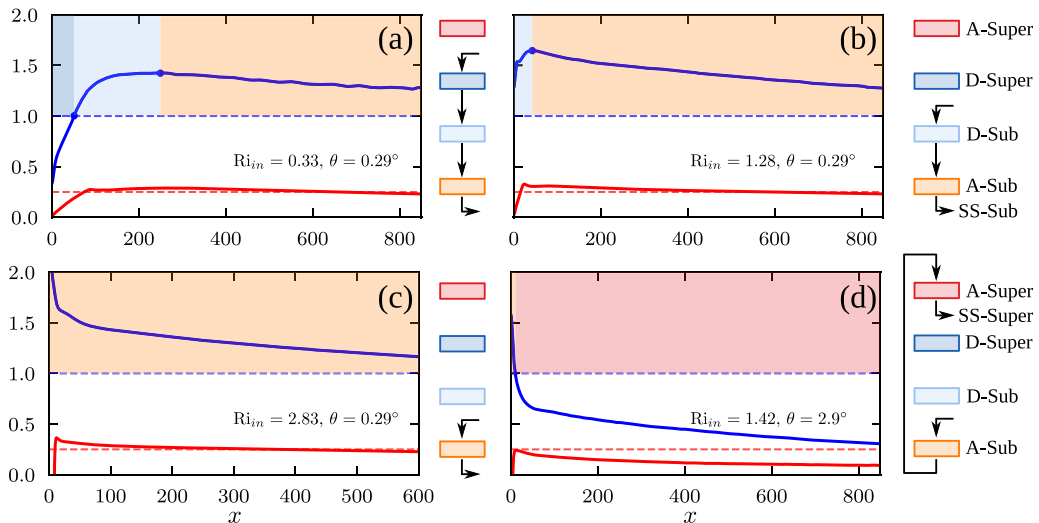


FIG. 6. Bulk Richardson number Ri (blue line) together with the local minimum of gradient Richardson number Ri_g at the interface layer (red line) for (a) case 3, (b) case 4, (c) case 5, and (d) case 6. Colors denote the non-normal regime at each streamwise location.

state, the intermediate layer prevents any exchange of momentum or concentration between the lower near-bed and the upper interface layers. The main point to be stressed is that, when the current is rapidly varying, the interface becomes highly turbulent (spanwise coherent KH vortices appear) and the intermediate layer disappears. As a result, there is vertical transport between the near-bed and interface layers. One could consider the intermediate layer as a “gate” that opens the path for momentum, concentration, and turbulence exchange between the layers in the rapidly varying state, when the current is away from its self-similar state. This transport between the layers is accounted for by the interface term $\overline{w'c}|_{z_{um}}$.

VII. OTHER CASES

The spatial evolution of the bulk Richardson number for the other four cases is shown in Fig. 6. Cases 3, 4, and 5 consider a subcritical slope and in all these cases, after the initial rapid evolution, the current slowly evolves to the same self-similar subcritical state. In case 3, the current at the inlet starts in the supercritical state. In case 4, the current at the inlet starts at about the same Richardson number as the self-similar state. However, since the structure of the mean flow and turbulence at inlet are different from the self-similar structure, the current goes through an initial phase of rapid evolution. In case 5, the inlet is more subcritical than the self-similar state and the current goes through an initial phase of rapid acceleration followed by slow acceleration towards the self-similar state. It is clear that, no matter where you enter the cycle, it will follow the natural cyclic evolution until all the balances (mean momentum, turbulence, and concentration flux) are nearly achieved, so that the current can slowly evolve towards its SS state.

Case 6 is particularly interesting, because its supercritical slope is the same as the downstream slope of the slope-break case 2. Thus, in both these cases, far downstream the current reaches the same self-similar supercritical state. However, the bulk Richardson number evolution shown in Fig. 6(d) is quite different from that shown in Fig. 1(b). The difference is in the nature of turbulence as the flow enters the supercritical slope. In case 6, although the bulk Reynolds number of the current at the inlet was chosen to be subcritical, the inflow was designed such that there was turbulence in the interface layer. This allowed the current to go through a very rapid evolution through the A-Sub state to quickly become A-Super. After a short duration of rapid evolution in the A-Super state,

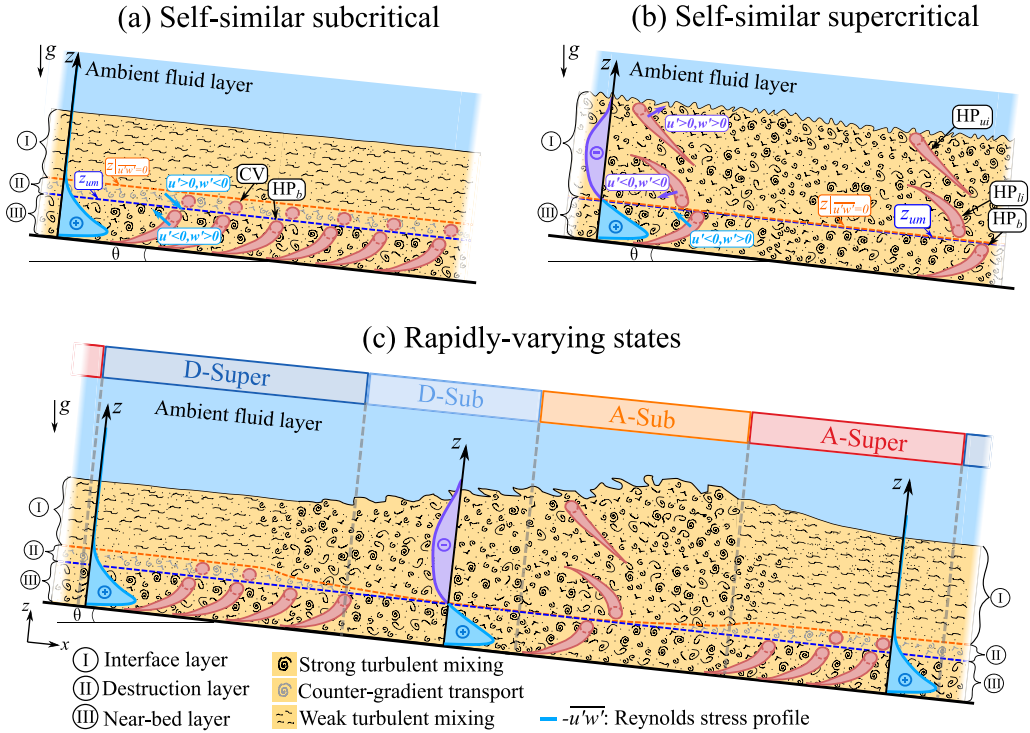


FIG. 7. Schematic representation of the near-bed and interfacial turbulence for (a) self-similar supercritical currents, (b) self-similar subcritical currents, and (c) rapidly varying states. In blue dashed line: z_{um} ; in orange dashed line: vertical location where $u'w' = 0$. We note that in (c) the D-Sub and A-Sub states have been stretched in the streamwise direction for ease of visualization.

the current enters a period of slow evolution towards the self-similar state, whereas, in case 2, the current as it entered the steeper slope was without any significant production of turbulence in the interface layer. Thus, as the current accelerated and entered the A-Super state, for lack of turbulence in the interface layer, it could not enter a slow evolution towards the self-similar state. The current had to evolve through a cycle of deceleration in order to develop turbulence in the interface layer. Once turbulence is generated in the interface layer, the current is able to go through the A-Super state and evolve towards the self-similar state. Cases 2 and 6 clearly illustrate the fact that the bulk Richardson number alone is not sufficient to characterize the state of the flow at the inlet. Depending on the nature of turbulence, especially in the interface layer, different evolutions of the current are possible. In summary, the four additional cases shown in Fig. 6 illustrate the important point that no matter which state the current enters the domain, the cyclic evolution through the four states applies as the current settles to its self-similar state. Inlet conditions far away from this state will provoke the current to undergo a rapid transition often accompanied by hydraulic jumps, as seen experimentally by [45,46].

VIII. DISCUSSION AND CONCLUSIONS

The self-similar supercritical (SS-Super), self-similar subcritical (SS-Sub), and rapidly varying currents that transition between subcritical and supercritical states are schematically represented in Fig. 7. Self-similar subcritical (SS-Sub) currents have a three layer structure [Fig. 7(b), Ref. [22]]: (i) an interface layer above the wall-normal location where Reynolds stress is zero (dashed orange line) and capped by the ambient fluid layer from above, (ii) an intermediate layer where TKE

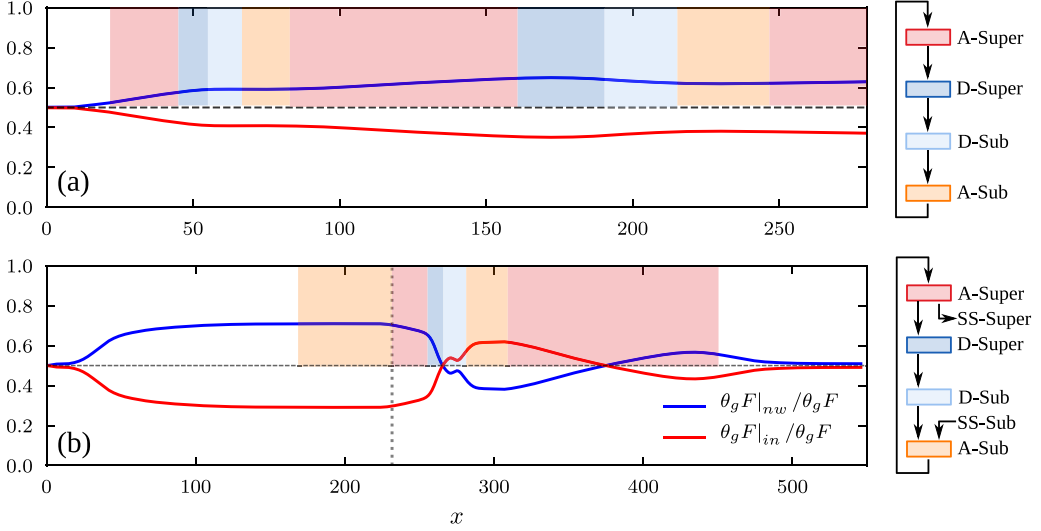


FIG. 8. Partitioning of concentration flux between the near-bed (blue line) and the interface (red line) layers for (a) case 1 and (b) case 2.

production is negative, located below the interface layer and above the maximum of streamwise velocity (dashed blue line), and (iii) a near-bed layer below the maximum of streamwise velocity. In this three-layer structure, counter-rotating vortices [CV in Fig. 7(b)] are spawned downstream of the near-bed hairpin vortex heads (HP_b). These CVs play a crucial role in establishing the countergradient transport of momentum and concentration in the intermediate layer and thereby strongly isolating the near-bed turbulence from penetrating into the interface layer.

In most shear flows, to the leading order, total production can be approximated as the shear TKE production defined as $\overline{P_s} = -\overline{u'w'} \frac{\partial \bar{u}}{\partial z}$. Asymmetry in the velocity profile near the velocity maximum results in a thin layer of fluid where Reynolds stress $-\overline{u'w'}$ and velocity gradient $\partial \bar{u} / \partial z$ have different sign. This region of negative turbulence production is termed the intermediate layer (II), between surface of \bar{z}_{um} marked in dashed blue and surface of $\bar{z}_{u'w'=0}$ marked in dashed orange. As a result, when stratification suppresses turbulence within the interface layer, negative TKE production is found right above the velocity maximum. Any turbulent fluctuations that enter this layer from below are converted back to mean flow shear and a strong stable concentration gradient [22].

Self-similar supercritical (SS-Super) currents are comprised of two layers: (i) a near-bed layer below the velocity maximum and (ii) an interface layer. These currents are populated by three families of hairpin vortices (HP_b , HP_{li} , and HP_{ui} , which are schematically represented in Fig. 7) [21]. Thus both the near-bed and the interface layers are vigorously turbulent. Thus, in the self-similar state, the streamwise momentum source is balanced by a combination of basal drag at the bottom of the bed and entrainment drag at the interface with the ambient clear fluid. For the supercritical slope $\theta = 2.9^\circ$, the breakdown of the momentum source between basal and entrainment drag is roughly balanced. In contrast, in the subcritical slope of $\theta = 0.29^\circ$, the breakdown between basal and entrainment drag is 75% and 25%.

Similar to turbulence partitioning between the near-bed and interface layers, we can also address concentration flux partitioning between the two layers. In the present context of conservative current, the total streamwise concentration flux [$\theta_g F = F + \int_0^\infty R\overline{u'c'}g \sin \theta dz$; see Eq. (8)] remains independent of the streamwise location x . This constant streamwise concentration flux is separated into flux contributions in the near-bed and interface layers. This concentration flux partitioning is presented in Fig. 8. In case 1, the inlet condition was such that concentration fluxes were

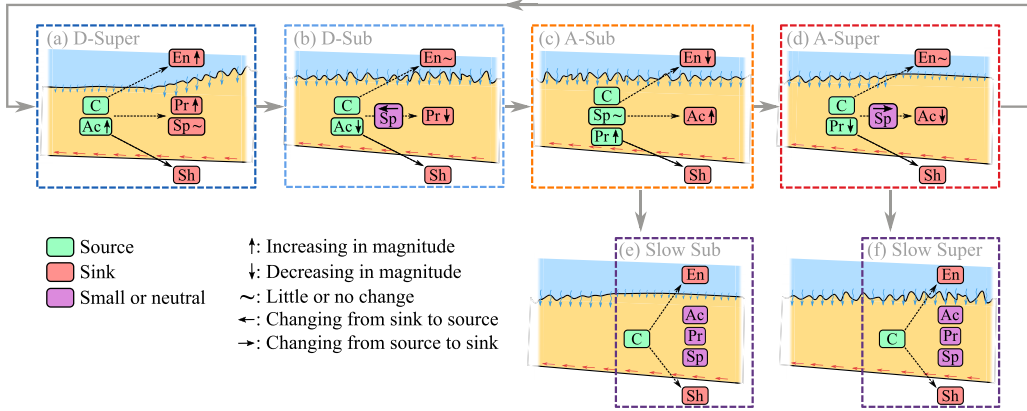


FIG. 9. Schematic momentum balance for (a) D-Super, (b) D-Sub, (c) A-Sub, (d) A-Super, (e) slow variation to SS-Sub, and (f) slow variation to SS-Super. The shown momentum balance terms are C, concentration, Ac, depth averaged acceleration, Pr, streamwise pressure gradient force, Sh, basal drag, En, ambient fluid entrainment, and Sp, depth averaged streamwise change of Reynolds stress.

equipartitioned between the two layers. However, soon the partitioning of concentration flux between the near-bed and interface layers is in the ratio 62% and 38%.

As the current cyclically evolves between the four states we observe the fraction of concentration flux contained in the near-bed layer to peak at about 65% with only 35% in the upper interface layer, when the current was in D-Super state. In this state, the interface layer is devoid of turbulence and thus cannot retain a larger concentration in suspension. We observe the opposite scenario in the A-Sub state where the fraction of concentration flux contained in the near-bed layer reaches the minimum value of about 60%. The higher fraction of 40% in the upper interface layer is due to the action of vigorous turbulence in the upper layer. The observed variation as the current cycles through the different states is quite small, since the effect on concentration flux exchange between the layers is not very strong. In case 2 also at the inlet the concentration flux was applied equipartitioned between the two layers. However, the flow quickly partitioned to about 70% and 30% corresponding to the bed slope of $\theta = 0.29^\circ$. Following slope change (marked by the vertical dashed line) there is vigorous exchange of concentration flux between the two layers and for $x > 500$ concentration flux settles to about 50% in each layer corresponding to the supercritical slope. It should be noted that, although equipartitioning was achieved at earlier time instances, the current continued to evolve and exchange concentration between the layers, since a slow approach to perfect self-similarity could be achieved after going through the deceleration phase.

The momentum balance during the cyclic evolution of the current is schematically denoted in Fig. 9 for case 1. In all the states, the momentum source due to concentration varies little. The momentum source is primarily balanced by basal drag and entrainment drag at the interface with the clear fluid. While variation in the basal drag is quite small, entrainment drag remains a sink (negative value) and exhibits oscillation. Entrainment drag increases in magnitude during D-Super, remains at the higher value during the D-Sub state, decreases during the A-Sub state, and again remains nearly a constant at the lower value during the A-Super state. The increased entrainment is associated with an unstable and turbulent interface layer, while the lower entrainment is during a period when the interface is stable and free of turbulence. In the self-similar state, entrainment drag is high in the supercritical state and low in the subcritical state. However, as discussed above, this is not true when the flow is undergoing rapid evolution. The structure of the interface layer in the A-super and D-sub states does not resemble those of self-similar supercritical and subcritical currents.

For the other terms of the momentum balance, we start the investigation at the D-Sub state, where flow deceleration acts as a momentum source (term denoted as A_c), but its magnitude is decreasing as indicated by the downward pointing black arrow. The behavior of the pressure term is exactly opposite of the acceleration contribution and it is typically lower in magnitude. In the A-Sub state, due to flow acceleration A_c becomes a sink, while the pressure term becomes a source and both increase in magnitude. In the A-Super state, acceleration and pressure terms remain sink and source, respectively, but their magnitudes start decreasing as indicated by the down arrows. The Reynolds stress contribution also changes sign. It is negative and remains nearly a negative constant in the D-Super state, then increases during D-Sub to become positive, remains a positive constant during A-Sub, and completes the cycle by decreasing to negative values during A-Super. The evolution is such that during transitions between supercritical and subcritical states the current briefly reaches normal states where the acceleration, pressure, and Reynolds stress contributions are nearly zero.

While the currents at self-similar state preserve their three/two layer structure as they travel downstream, under rapidly varying conditions the current constantly undergoes readjustment of turbulence and momentum balance. The evolution in case 2 is similar, except that, as the slope increases, the magnitude of the momentum source also increases. Correspondingly the basal drag and interfacial entrainment drag also increase in magnitude and all these changes are associated with superposed oscillations.

From the present work we draw the following key conclusions for both gravity and conservative turbidity currents.

(1) While flow conditions in the self-similar regime are solely determined by the bed slope, the rapidly varying transition to it depends on the initial upstream condition.

(2) A rapidly varying current naturally evolves through the following cyclic sequence: \dots A-Sub \rightarrow A-Super \rightarrow D-Super \rightarrow D-sub \rightarrow A-Sub $\rightarrow \dots$. Here, “D” and “A” means that the current is decelerating and accelerating, “Sub” indicates $Ri > 1$, and “Super” indicates $Ri < 1$.

(3) For bed slopes $\theta > 1^\circ$, the current eventually slowly accelerates to a self-similar supercritical (SS-Super) state. For bed slopes $\theta < 1^\circ$, the current eventually slowly evolves to a self-similar subcritical (SS-Sub) state. Depending on the status of the current at the inlet, the current will evolve through the cyclic sequence of rapid variation before entering slow evolution towards the self-similar state. For intermediate slopes $\theta \approx 1^\circ$ the current is transcritical and the current is observed to go through the cyclic sequence several cycles without settling to a self-similar state.

(4) The bulk Richardson number of the current at the inlet only characterizes the state of mean velocity and concentration profiles and thus is not sufficient to determine how the current will evolve towards its eventual self-similar state. The turbulence initially present in the interface layer (or lack of it) also plays a crucial role. Similarly, during rapid deceleration a supercritical current may quickly become subcritical in terms of the mean flow; however, the turbulent state of the current may still exhibit the two-layer layer structure of the supercritical state. This mismatch is the reason why the current continues to cyclically evolve through the four different states.

(5) In the depth-averaged streamwise momentum balance, the source term due to concentration varies little and is mainly balanced by basal drag and entrainment drag at the current’s interface. While the former remains almost a constant between the rapidly varying states, the latter shows substantial variation influenced by the amount of turbulence present in the interface. The balance is then achieved by the presence of the acceleration and pressure terms, which during deceleration states act as a source and a sink of streamwise momentum, respectively. During acceleration states, the opposite is true [see Figs. 5(a), 5(b) and Fig. 9].

(6) In self-similar states depth-averaged TKE production is nearly completely balanced by TKE dissipation. However, in the rapidly varying states, dissipation lags production, and this imbalance results in streamwise advection of TKE and expenditure of vertical Reynolds flux [see Figs. 5(c) and 5(d)].

(7) During rapidly varying states, there is an imbalance in the carrying capacity of the near-bed and interfacial layers, which results in concentration exchange between the two layers [Figs. 5(e) and 5(f)].

ACKNOWLEDGMENTS

The authors would like to thank ExxonMobil for their support. S.L.Z. and M.I.C. would also like to acknowledge CONICET, CNEA, and UNCuyo.

-
- [1] J. S. Salinas, M. I. Cantero, M. Shringarpure, and S. Balachandar, Properties of the body of a turbidity current at near-normal conditions: 1. Effect of bed slope, *J. Geophys. Res.: Oceans* **124**, 7989 (2019).
 - [2] J. S. Salinas, M. I. Cantero, M. Shringarpure, and S. Balachandar, Properties of the body of a turbidity current at near-normal conditions: 2. Effect of settling, *J. Geophys. Res.: Oceans* **124**, 8017 (2019).
 - [3] G. Parker, Y. Fukushima, and H. M. Pantin, Self-accelerating turbidity currents, *J. Fluid Mech.* **171**, 145 (1986).
 - [4] G. Parker, M. García, Y. Fukushima, and W. Yu, Experiments on turbidity currents over an erodible bed, *J. Hydraul. Res.* **25**, 123 (1987).
 - [5] J. S. Salinas, S. Zúñiga, M. Cantero, M. Shringarpure, J. Fedele, D. Hoyal, and S. Balachandar, Slope dependence of self-similar structure and entrainment in gravity currents, *J. Fluid Mech.* **934**, R4 (2022).
 - [6] M. García and G. Parker, Experiments on the entrainment of sediment into suspension by a dense bottom current, *J. Geophys. Res.* **98**, 4793 (1993).
 - [7] C. J. Dallimore, J. Imberger, and T. Ishikawa, Entrainment and turbulence in saline underflow in Lake Ogawara, *J. Hydraul. Eng.* **127**, 937 (2001).
 - [8] F. Necker, C. Härtel, L. Kleiser, and E. Meiburg, High-resolution simulations of particle-driven gravity currents, *Int. J. Multiphase Flow* **28**, 279 (2002).
 - [9] R. L. Fernandez and J. Imberger, Bed roughness induced entrainment in a high Richardson number underflow, *J. Hydraul. Res.* **44**, 725 (2006).
 - [10] M. Cantero, J. R. Lee, S. Balachandar, and M. García, On the front velocity of gravity currents, *J. Fluid Mech.* **586**, 1 (2007).
 - [11] O. E. Sequeiros, H. Naruse, N. Endo, M. H. García, and G. Parker, Experimental study on self-accelerating turbidity currents, *J. Geophys. Res.: Oceans* **114**, C05025(2009).
 - [12] M. A. Islam and J. Imran, Vertical structure of continuous release saline and turbidity currents, *J. Geophys. Res.: Oceans* **115**, C08025(2010).
 - [13] J. S. Salinas, T. Bonometti, M. Ungarish, and M. I. Cantero, Rotating planar gravity currents at moderate Rossby numbers: Fully resolved simulations and shallow-water modelling, *J. Fluid Mech.* **867**, 114 (2019).
 - [14] J. S. Salinas, M. I. Cantero, E. A. Dari, and T. Bonometti, Turbulent structures in cylindrical density currents in a rotating frame of reference, *J. Turbul.* **19**, 463 (2018).
 - [15] B. Kneller, M. M. Nasr-Azadani, S. Radhakrishnan, and E. Meiburg, Long-range sediment transport in the world's oceans by stably stratified turbidity currents, *J. Geophys. Res.: Oceans* **121**, 8608 (2016).
 - [16] E. Meiburg and B. Kneller, Turbidity currents and their deposits, *Annu. Rev. Fluid Mech.* **42**, 135 (2010).
 - [17] M. Cantero, S. Balachandar, and M. García, Highly resolved simulations of cylindrical density currents, *J. Fluid Mech.* **590**, 437 (2007).
 - [18] C. Cenedese and C. Adduce, Mixing in a density-driven current flowing down a slope in a rotating fluid, *J. Fluid Mech.* **604**, 369 (2008).
 - [19] O. E. Sequeiros, B. Spinewine, R. T. Beaubouef, T. Sun, M. H. García, and G. Parker, Characteristics of velocity and excess density profiles of saline underflows and turbidity currents flowing over a mobile bed, *J. Hydraul. Eng.* **136**, 412 (2010).
 - [20] O. E. Sequeiros, Estimating turbidity current conditions from channel morphology: A Froude number approach, *J. Geophys. Res.: Oceans* **117**, C04003(2012).
 - [21] J. S. Salinas, S. Balachandar, and M. I. Cantero, Control of turbulent transport in supercritical currents by three families of hairpin vortices, *Phys. Rev. Fluids* **6**, 063801 (2021).

- [22] J. S. Salinas, S. Balachandar, M. Shringarpure, J. Fedele, D. Hoyal, S. Zúñiga, and M. I. Cantero, Anatomy of subcritical submarine flows with a lutocline and an intermediate destruction layer, *Nat. Commun.* **12**, 1649 (2021).
- [23] J. Salinas, S. Balachandar, M. Shringarpure, J. Fedele, D. Hoyal, and M. Cantero, Soft transition between subcritical and supercritical currents through intermittent cascading interfacial instabilities, *Proc. Natl. Acad. Sci. U.S.A.* **117**, 18278 (2020).
- [24] M. García and G. Parker, Experiments on hydraulic jumps in turbidity currents near a canyon-fan transition, *Science* **245**, 393 (1989).
- [25] A. Fildani, W. R. Normark, S. Kostic, and G. Parker, Channel formation by flow stripping: Large-scale scour features along the monterey east channel and their relation to sediment waves, *Sedimentology* **53**, 1265 (2006).
- [26] S. Kostic, O. Sequeiros, B. Spinewine, and G. Parker, Cyclic steps: A phenomenon of supercritical shallow flow from the high mountains to the bottom of the ocean, *J. Hydro-Environ. Res.* **3**, 167 (2010).
- [27] W. Rodi, G. Constantinescu, and T. Stoesser, *Large-Eddy Simulation in Hydraulics* (CRC Press, Boca Raton, FL, 2013).
- [28] T. M. Özgökmen, T. Iliescu, and P. F. Fischer, Reynolds number dependence of mixing in a lock-exchange system from direct numerical and large eddy simulations, *Ocean Modell.* **30**, 190 (2009).
- [29] N. Jarrin, S. Benhamadouche, D. Laurence, and R. Prosser, A synthetic-eddy-method for generating inflow conditions for large-eddy simulations, *Int. J. Heat Fluid Flow* **27**, 585 (2006).
- [30] T. Okaze and A. Mochida, Cholesky decomposition-based generation of artificial inflow turbulence including scalar fluctuation, *Comput. Fluids* **159**, 23 (2017).
- [31] M. Lee and R. D. Moser, Direct numerical simulation of turbulent channel flow up to $Re_\tau \approx 5200$, *J. Fluid Mech.* **774**, 395 (2015).
- [32] S. Dong, G. E. Karniadakis, and C. Chrysosostomidis, A robust and accurate outflow boundary condition for incompressible flow simulations on severely-truncated unbounded domains, *J. Comput. Phys.* **261**, 83 (2014).
- [33] J. W. Miles, On the stability of heterogeneous shear flows, *J. Fluid Mech.* **10**, 496 (1961).
- [34] T. Ellison and J. S. Turner, Turbulent entrainment in stratified flows, *J. Fluid Mech.* **6**, 423 (1959).
- [35] R. M. Dorrell, J. Peakall, S. E. Darby, D. R. Parsons, J. Johnson, E. J. Sumner, R. B. Wynn, E. Özsoy, and D. Tezcan, Self-sharpening induces jet-like structure in seafloor gravity currents, *Nat. Commun.* **10**, 1381(2019).
- [36] M. H. García, Experimental study of turbidity currents, M.s. thesis, University of Minnesota, Minneapolis, 1985.
- [37] M. H. García, Depositing and eroding sediment-driven flows Turbidity currents, Ph.D. thesis, University of Minnesota, St. Anthony Falls Hydraulic Laboratory, 1990.
- [38] J. Zhou, R. Adrian, S. Balachandar, and T. Kendall, Mechanics for generating coherent packets of hairpin vortices in channel flow, *J. Fluid Mech.* **387**, 353 (1999).
- [39] P. Chakraborty, S. Balachandar, and R. Adrian, On the relationships between local vortex identification schemes, *J. Fluid Mech.* **535**, 189 (2005).
- [40] A. F. Hussain, Coherent structures and turbulence, *J. Fluid Mech.* **173**, 303 (1986).
- [41] M. M. Rogers and R. D. Moser, The three-dimensional evolution of a plane mixing layer: The Kelvin-Helmholtz rollup, *J. Fluid Mech.* **243**, 183 (1992).
- [42] M. Shringarpure, M. I. Cantero, and S. Balachandar, Dynamics of complete turbulence suppression in turbidity currents driven by monodisperse suspensions of sediment, *J. Fluid Mech.* **712**, 384 (2012).
- [43] I. Z. Naqavi, J. C. Tyacke, and P. G. Tucker, Direct numerical simulation of a wall jet: Flow physics, *J. Fluid Mech.* **852**, 507 (2018).
- [44] S. Kostic and G. Parker, The response of turbidity currents to a canyon-fan transition: Internal hydraulic jumps and depositional signatures, *J. Hydraul. Res.* **44**, 631 (2006).
- [45] Z. Nourmohammadi, H. Afshin, and B. Firoozabadi, Experimental observation of the flow structure of turbidity currents, *J. Hydraul. Res.* **49**, 168 (2011).
- [46] E. Khavasi, H. Afshin, and B. Firoozabadi, Effect of selected parameters on the depositional behaviour of turbidity currents, *J. Hydraul. Res.* **50**, 60 (2012).